JOURNAL OF THERMOPHYSICS AND HEAT TRANSFER
Vol. 21, No. 4, October–December 2007

Heat Transfer in Loop Heat Pipe's Wick: Effect of Porous Structure Parameters

Chuan Ren,* Qing-Song Wu,† and Mao-Bin Hu‡
University of Science and Technology of China, 230026 Hefei, Anhui, People's Republic of China

DOI: 10.2514/1.28122

The capillary-driven flow with conductive, convective, and evaporative heat transfer occurs in the capillary wick of a loop heat pipe after startup. An axisymmetric two-dimensional mathematical model, which considers adequately the capillary-driven convection as well as the effect of the interaction between the flowfield and the liquid–vapor interface on the position of the interface and the curvature of menisci, is developed to investigate the effect of porous structure parameters on the wick's performances without gravity. In this paper, the relation among porosity, effective pore radius, and permeability is considered while the effective thermal conductivity is adjusted to be numerically independent of them. It is shown that permeability associated with porosity and effective pore radius has little influence on the heat transfer performance but has strong influence on the driving performance.

Nomenclature

A_s	=	area of a close-contacted heated fin, m^2
c	=	special thermal capacity ($J/kg \cdot K$)
h	=	enthalpy, J/kg
K	=	permeability, m^2
k	=	thermal conductivity, $W/(m \cdot K)$
$\dot{m}$	=	mass flow rate of the working fluid, kg/s
$\boldsymbol{n}$	=	normal vector on the liquid–vapor interface
p	=	pressure, Pa
q	=	heat flux, W/m^2
R	=	radius of menisci's curvature, m
$\boldsymbol{r}$	=	position vector of meniscus, m
r_p	=	effective pore radius, m
$\boldsymbol{s}$	=	displacement vector of interface, m
T	=	temperature, K
t	=	time, s
U	=	total heat transfer coefficient, $W/(m^2 \cdot K)$
$\boldsymbol{V}$	=	velocity vector of infiltration, m/s
β_p	=	expansion coefficient with constant temperature, $1/Pa$
β_T	=	expansion coefficient with constant pressure, $1/K$
θ	=	contact angle between liquid and solid surface, deg
λ	=	latent heat of evaporation, J/kg
μ	=	dynamic viscosity, $kg/(m \cdot s)$
ν	=	kinematic viscosity, m^2/s
ρ	=	density, kg/m^3
σ	=	coefficient of surface tension, N/m
ϕ	=	porosity

Subscripts

c	=	capillary
e	=	reference
eva	=	evaporation
f	=	fluid
g	=	vapor
in	=	inlet
l	=	liquid
n	=	in the normal direction
out	=	outlet
r	=	in the radial direction
s	=	saturated
t	=	total
wall	=	on the heated wall
z	=	in the longitudinal direction

Received 30 September 2006; revision received 9 March 2007; accepted for publication 3 May 2007.

*Doctor, Department of Thermal Science and Energy Engineering; renc@mail.ustc.edu.cn.

†Professor, Department of Thermal Science and Energy Engineering; qswu@ustc.edu.cn (Corresponding Author).

‡Post Doctor, Department of Thermal Science and Energy Engineering.

Introduction

IN THE past decades, because of the demand in thermal management of advanced satellites and spacecrafts as well as cooling of electrical and electronic devices, two heat transfer devices have been developed and tested [1–6], the so-called capillary pumped loop (CPL) and the loop heat pipe (LHP), which depend on evaporation to absorb heat load and capillary force developed on menisci to drive a working fluid to flow and transfer heat over large distance. Kaya and Hoang [1] developed a one-dimensional mathematical model based on the pressure drop calculation along the fluid path in the LHP and the steady-state energy conservation equations in the convection or radiation environment. They simulated the steady-state performance of a LHP at different input powers and different sink temperatures by this model while two separate LHPs were tested in NASA's Geoscience Laser Altimeter System (GLAS) and the U.S. Naval Research Laboratory (NRL). The comparison between the calculations and the experimental results showed good agreement (within 5%), indicating that this model proved to be a useful tool for reliable prediction of the steady-state performance of the LHP at the input power of 100–800 W. Ku [2] analyzed the experimental results of the GLAS/NRL LHPs, investigated operating characteristics of LHPs, and attempted to explain the temperature hysteresis and temperature overshoot during startup. Pouzet et al. [3] designed an experimental CPL and developed a global one-dimensional mathematical model including all elements and physical processes to investigate a dynamic response of a CPL at various heat loads. They simulated satisfactorily the following steps to the applied heat load and the damped oscillations of low frequency observed between the condenser and the reservoir, but failed to simulate the self-sustained oscillations of higher frequencies. Zhang et al. [4] carried out some ground tests of the LHP startup in different conditions to investigate the effects of different conditions on the startup behaviors of LHPs and the effect of the startup on the steady-state operation of LHPs. Vasiliev [5] and Maydanik [6] reviewed the design, history, and current advance of LHPs in 2005. Most of the previous researches focused on tests or simulations of the whole device, so many important properties of evaporators were neglected. The evaporator with the capillary

porous structure is the primary functional component which accepts heat fluxes, organizes evaporation, and produces the driving force of the working fluid flowing circularly in the whole device. Heat transfer with coupled flow and evaporation occurs just in the capillary porous structure. For the security and efficiency of the LHPs performance, it is important and necessary to investigate the dynamic and thermodynamic behavior of the working fluid in the capillary porous structure. Kaya and Hoang [1] and Pouzet et al. [3] thought for predicting more accurately the steady-state performance of a LHP and investigating further the instability of a CPL that it was necessary to focus on the evaporator and investigate the physical processes in the capillary porous structure of a CPL/LHP.

Others focused directly on the evaporator with the capillary wick. Cao and Faghri [7] developed a two-dimensional mathematical model for heat transfer in the capillary wick and the cover plate with three-dimensional vapor flow in the groove, and they [8] obtained the two-dimensional analytical solutions of flow and heat transfer in the capillary wick based on the Laplace-type equation for pressure and the perturbation method for temperature. By using the Green's function method, LaClair and Mudawar [9] developed a one-dimensional approximate solution without convection for the coupled liquid core, capillary wick, and metal shell to investigate the startup behavior of a CPL evaporator. But these papers considered the capillary wick as a fully liquid-saturated wick with the liquid–vapor interface fixed at the surface of the wick. Demidov and Yatsenko [10] developed a two-dimensional mathematical model considering both convection and the free liquid–vapor interface in the wick, and investigated numerically steady capillary-driven flow and heat transfer in rectangular porous media. Khrustalev and Faghri [11] developed a one-dimensional mathematical model on the basis of heat transfer with thin-film evaporation theory in a pore and heat transfer in the dry porous media and close-touched heated fins (or flat), and the analytical steady solution was derived. Figus et al. [12] developed two two-dimensional mathematical models separately based on the Darcy model and the pore network model, both of which considered the moving liquid–vapor interface in the wick and no convection in the energy equations, to study steady heat transfer in the wick with a single or varying pore-size distribution. Zhao and Liao [13] investigated experimentally heat transfer in glass-bead-packed cubic porous media with a groovy heated wall on the top at different heated fluxes, and the one-dimensional approximate solutions derived from this paper agreed with the experimental results. Kaya and Goldak [14] used the mathematical model and boundary conditions similar to Demidov and Yatsenko's [10] to investigate heat and mass transfer in the capillary structure of a LHP. By using the method based on the cluster nucleation theory to calculate the boiling limit in a porous structure, they clarified that the capillary limit is always before the boiling limit in a porous structure and that it is the sole limit of operating a LHP. All of these papers [10–14] stayed at the simulation or experiments of steady heat transfer in the capillary wick while current researches on CPLs/LHPs focus on transient characters [3–6]. We developed an axisymmetric two-dimensional mathematical model to simulate steady/transient heat transfer with flow and evaporation in the capillary wick of a LHP [15]. This model considers adequately the capillary-driven convection as well as the effect of the interaction between the flowfield and the liquid–vapor interface on the position of the interface and the curvature of menisci, that is, the capillary force.

Generally, a wick's performances are evaluated in three aspects: the driving performance, the heat transfer performance, and the capillary effect of evaporation. As the LHP is a self-driving two-phase heat transfer device, "the driving performance" is introduced to characterize the ability related to a self-driving operation, such as the pressure field, the capillary-driven flow of the working fluid, and the heat transfer limit. The heat transfer performance evaluates the heat transfer efficiency. The capillary effect of evaporation is related to the difficulty of organizing evaporation in the capillary porous structure. Besides heat flux, the wick's working state and performances are influenced by many factors. They are classified into three kinds: 1) the outer parameters, such as inlet pressure, inlet temperature, and outlet pressure; 2) the parameters related to the porous structure, such as porosity, effective pore radius, permeability, and effective thermal conductivity; 3) properties of the working fluid, such as viscosity and latent heat of evaporation. Khrustalev and Faghri [11] studied numerically the effects of heat flux and effective pore radius on the thickness of the vapor blanket, the overall heat transfer coefficient, and the fin superheat on the basis of thin-film evaporation and one-dimensional assumption. Liao and Zhao [16] investigated experimentally the effects of heat flux, particle size, inlet temperature, and adverse hydrostatic head on the total heat transfer coefficient and the critical heat flux in the case of evaporative or boiling heat transfer. Assuming convection was neglected, Hanlon and Ma [17] investigated experimentally and numerically the effects of heat flux and the porous structure's thickness on temperature, the evaporative heat transfer coefficient, the capillary and boiling limit, as well as some factors related to the critical heat flux.

Because of the porous structure, porosity, the effective pore radius, permeability, and the effective thermal conductivity are interactive parameters. Although it is attractive for researchers and engineers to understand the effect of each parameter on a wick's working state and performances, it is difficult to adjust each parameter in experiments. Fortunately, this can be realized in numerical simulation. In this paper, this model developed in [15] is used to investigate the effect of porous structure parameters on a wick's performances without gravity. The effect of the effective thermal conductivity on a wick's performances has been presented in [18]. In this paper, keeping the effective thermal conductivity constant or numerically "independent" of others, the effect of permeability associated with porosity and the effective pore radius on a wick's performances is investigated in detail.

Mathematical Model and Numerical Simulation

The evaporator of 16 mm in diameter, investigated in this paper, has the primary wick, the second wick, eight deeper longitudinal grooves, and plenty of shallower azimuthal grooves in its shell wall. The configuration is illustrated in Fig. 1. The primary wick is 5 mm thick in the radial direction and is made of sintered nickel powders with the effective pore radius of 0.001 mm and porosity of 0.5. The width of an azimuthal groove is 1 mm, and so the width of a heated fin is. In our simulation, a cell shown in Fig. 2 is used to represent the entire primary wick because of the periodic heated boundary on the top and the geometrical and physical symmetry. It is 5 mm thick in the radial direction and 1 mm wide in the longitudinal direction.

Some assumptions are introduced as follows: 1) there is an homogeneous, isotropic, and rigid capillary porous medium, and the fluids are slightly compressible. 2) The properties for solid, liquid, and vapor are constant. 3) Gravity, heat radiation, and viscous dissipation are neglected, and there is no inner heated source. 4) There is axisymmetric flow to the evaporator's axis. 5) Local

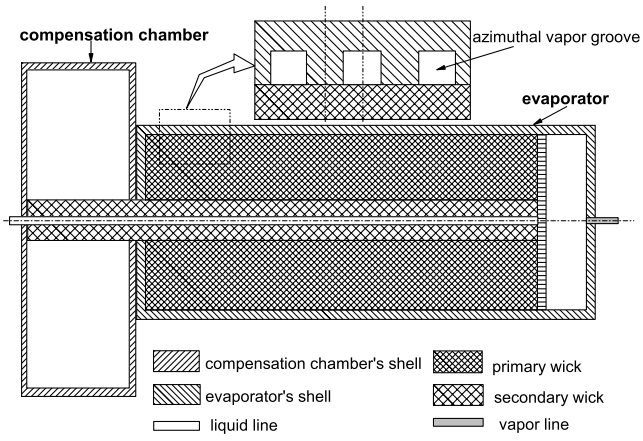

Fig. 1 Configuration of the evaporator with azimuthal grooves and the compensation chamber.

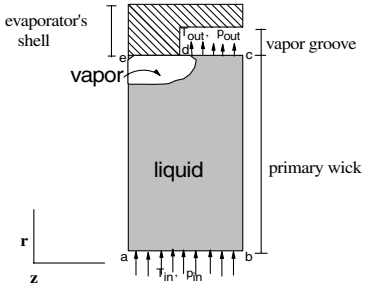

Fig. 2 Diagram of the cell for simulation with the width of half-fin and half-groove.

thermal equilibrium exists between the solid and fluid phases. 6) Evaporation occurs on the liquid–vapor interface, and no boiling occurs in the liquid.

The continuum equation (1), Darcy's law (2), and the equation of state (3) are listed below:

$$\frac{\partial}{\partial t}(\rho_f \phi) + \nabla \cdot (\rho_f \boldsymbol{V}) = 0 \tag{1}$$

$$\boldsymbol{V} = -\frac{K}{\mu}\nabla p \tag{2}$$

$$\rho_f = \rho_{o,f}[1 - \beta_{T,f}(T - T_e) + \beta_{p,f}(p - p_e)], \qquad f = l, g \tag{3}$$

Combining Eq. (1) with Eqs. (2) and (3), the pressure equation in cylindrical polar coordinates is derived as

$$\frac{\phi}{K}\frac{\partial}{\partial t}[\rho_{0,f}\beta_{p,f}(p - p_e)] - \frac{1}{r}\frac{\partial}{\partial r}\left(\frac{r}{\nu_f}\frac{\partial p}{\partial r}\right) - \frac{\partial}{\partial z}\left(\frac{1}{\nu_f}\frac{\partial p}{\partial z}\right) = -\frac{\phi}{K}\frac{\partial}{\partial t}\{\rho_{0,f}[1 - \beta_{T,f}(T - T_e)]\} \tag{4}$$

where ϕ, K, μ, and ν_f are porosity, permeability, the dynamic and kinematic viscosities, respectively. ρ_f, P, and $\boldsymbol{V}$ are the density of fluid, the pressure, and the velocity vector of infiltration, respectively. $\beta_{T,f}$ and $\beta_{p,f}$ are the expansion coefficients with constant pressure and temperature, respectively. And the subscripts l and g indicate liquid and vapor, respectively.

According to the assumptions, the enthalpy equation for coupled solid and fluid phases in cylindrical polar coordinates is derived as

$$\frac{\partial}{\partial t}(\rho_t h_f) + \frac{1}{r}\frac{\partial}{\partial r}(r\rho_f V_r h_f) + \frac{\partial}{\partial z}(\rho_f V_z h_f) = \phi\frac{\partial p}{\partial t} + V_r\frac{\partial p}{\partial r} + V_z\frac{\partial p}{\partial z} + \frac{1}{r}\frac{\partial}{\partial r}\left[rk_t\frac{\partial}{\partial r}\left(\frac{h_f - h_{0,f}}{c_{p,f}}\right)\right] + \frac{\partial}{\partial z}\left[k_t\frac{\partial}{\partial z}\left(\frac{h_f - h_{0,f}}{c_{p,f}}\right)\right] \tag{5}$$

where V_r and V_z are the velocity of infiltration in the radial and longitudinal directions, respectively. ρ_t is the total density of coupled solid and fluid phases, k_t is the effective thermal conductivity, and h_f is the enthalpy of fluid.

$$\rho_t \equiv \phi\rho_f + (1 - \phi)\rho_s\frac{c_s}{c_{p,f}} \tag{6}$$

$$h_f = h_{0,f} + c_{p,f}(T - T_e) \tag{7}$$

The boundary conditions (listed in the Appendix) are the same as those in [15,18]. The saturated liquid lies on the entrance with the inlet temperature $T_{\text{in}} = 293$ K and the inlet pressure $P_{\text{in}} = 882,500$ Pa while the outlet pressure is simplified to the value of $P_{\text{out}} = 882,500$ Pa. Before startup, pressure and temperature are homogeneous in the full liquid-saturated porous medium and the working fluid is saturated and resting.

The jump of pressure on the liquid–vapor interface in capillary porous media is as follows:

$$p_g|_{s(\boldsymbol{r},t)} - p_l|_{s(\boldsymbol{r},t)} = p_c \tag{8}$$

where p_c is the capillary force calculated by the Kelvin equation [19,20].

The conservation of energy on the liquid–vapor interface in porous media is as follows:

$$\rho_g h_g\left(\phi\frac{d\boldsymbol{s}(\boldsymbol{r},t)}{dt} - \boldsymbol{V}_g\right)\boldsymbol{n} + \left(k_t\frac{\partial T}{\partial n}\right)_g = \rho_l h_l\left(\phi\frac{d\boldsymbol{s}(\boldsymbol{r},t)}{dt} - \boldsymbol{V}_l\right)\boldsymbol{n} + \left(k_t\frac{\partial T}{\partial n}\right)_l \tag{9}$$

where $\boldsymbol{s}(\boldsymbol{r}, t)$ and $d\boldsymbol{s}(\boldsymbol{r}, t)/dt$ are the displacement and velocity of the interface, respectively. By using Eq. (9), the velocity and displacement of the interface are derived as

$$\frac{ds_n}{dt} = \frac{(\rho_l h_l V_{n,l} - \rho_g h_g V_{n,g}) - (k_{t,l}\frac{\partial T}{\partial n}|_l - k_{t,g}\frac{\partial T}{\partial n}|_g)}{\phi(\rho_l h_l - \rho_g h_g)} \tag{10}$$

$$s_n = s_n^0 + \frac{ds_n}{dt}\cdot\Delta t \tag{11}$$

In this model, a staggered background mesh of 100×20 with a local thin grid in the radial direction is introduced. The finite volume method is introduced to discretize the pressure equation (4) and the enthalpy equation (5), respectively, in the liquid and the vapor regions while the boundary conditions are treated as in [21]. The capillary force is treated as the inner boundary on the basis of Eq. (8). The discretized Eqs. (4) and (5) are treated separately by the strong implicit procedure (SIP) [21] method and coupled together in every time step while an explicit front tracking method with Eqs. (10) and (11) is used. The results are essentially independent of the number of grids, and the mathematical model and numerical simulation are reliable with the maximum iterative error less than 10^{-3}. The steady state is reached when the maximum relative change of both pressure and temperature among continuous transient states is less than 10^{-6}. (More details of the mathematical model have been presented in [15].)

Results and Discussion

General Simulation

The patterns of steady flowfields at different heat fluxes are qualitatively similar, but there are differences in the magnitude. An example at $q = 20,000$ W/m^2 is presented in Figs. 3 and 4. Pressure decreases gradually along the radial direction from the entrance to the interface and jumps up on the interface. Discontinuous pressure on the interface indicates the capillary force which is the driving force of a LHP. There lies a steady vapor blanket between the liquid-saturated zone in porous media and the close-touched heated fins for a definite interval of heat fluxes [11], but vapor blankets at low or moderate heat fluxes are too thin to be observed in experiments [13]. Our results agree with those of [11,13]. As results of the field of pressure, fluid flows fully in the radial direction in most regions of the wick whereas two-dimensional flow only occurs in the vicinity of heated fins and grooves. The radial velocity decreases along the radial direction in most regions due to the enlargement of the flowing area along the radial direction, then increases in the vicinity of heated fins because the effect of evaporation is stronger than the effect of the enlargement of the flowing area.

As shown in Fig. 3b, temperature increases along the radial direction from the entrance to the heated fins while there are two-dimensional patterns of isotherms in the vicinity of heated fins and grooves. For a metal wick with high thermal conductivity, its metal framework constitutes a channel net of heat flux which diffuses heat around from the heat source. So evaporation occurs everywhere on

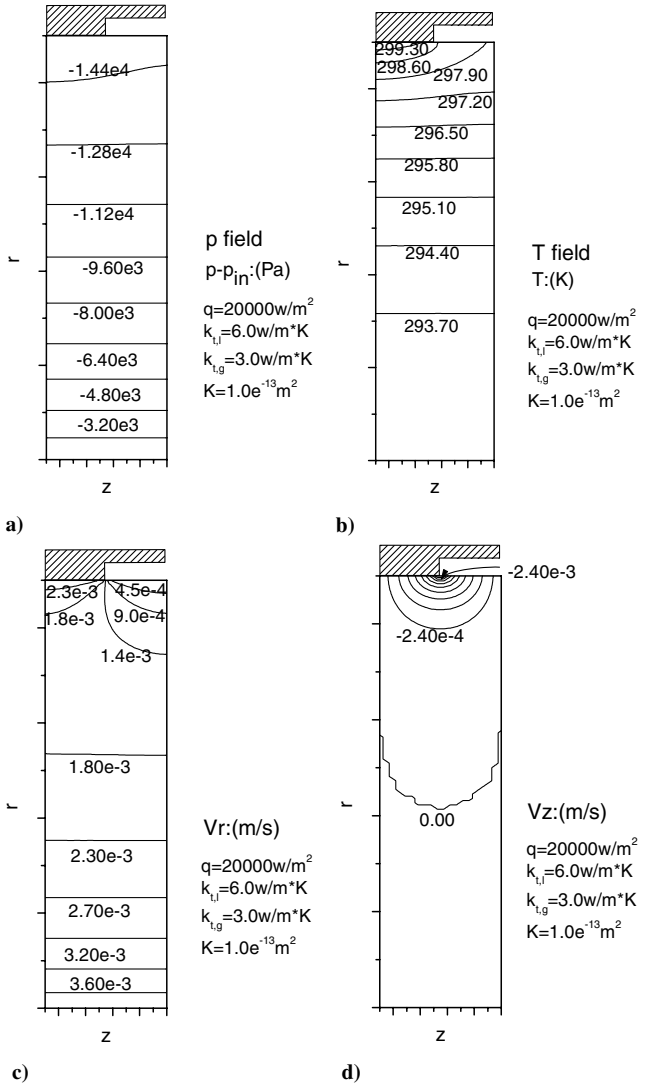

Fig. 3 Isogram of steady state at $q = 20,000$ W/m^2 (the radial thickness of 5 mm and the longitudinal width of 1 mm): a) pressure, b) temperature, c) radial velocity, and d) longitudinal velocity.

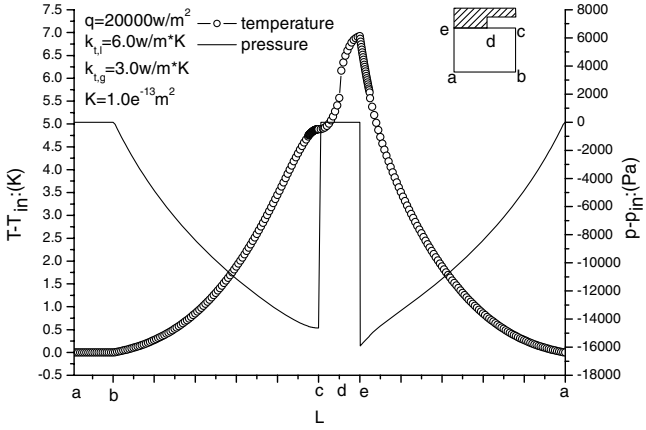

Fig. 4 Profiles of pressure and temperature along the boundary of steady state at $q = 20,000$ W/m^2.

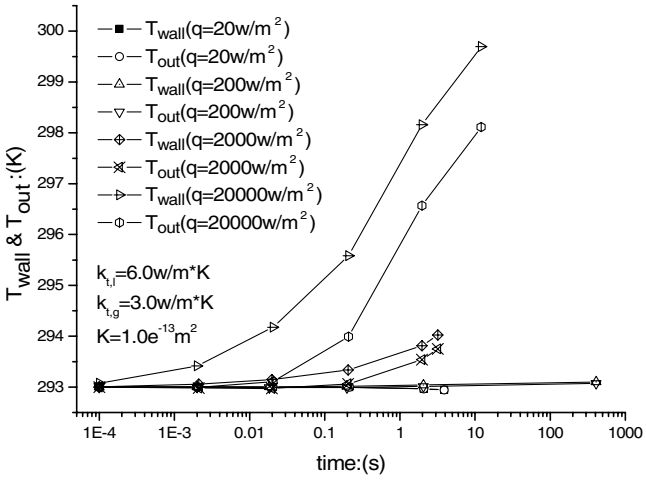

Fig. 5 Variation of mean temperatures T_{wall} and T_{out} versus time after startup at different heat fluxes.

the liquid–vapor interface in porous media including the section far from the heat source where evaporating energy is local heat. The results are coincident to those of [10,14] but different from those of [12] which assumed that no evaporation occurred on the interface between the vapor groove and the liquid-saturated wick. As shown in Fig. 4, temperature rises slightly along the boundary c–d where the region with scarce heat support lies. The profile of temperature has a steep slope at point d, which indicates that there lies a thin vapor blanket between the heated fin and the liquid-saturated zone in porous media. The distribution of radial velocities on the interface indicates the intensity of evaporation. The closer the region is to the center of the heat source, the more intensely it is vaporizing.

The variations of the mean fin temperature T_{wall} and the mean outlet temperature T_{out} versus time after startup at different heat fluxes are shown in Fig. 5. The magnitude of temperature increases with heat flux increasing. The temperature difference between T_{wall} and T_{out} changes little when it approaches the steady state. With a log scale on the time axis, one can see that the variation of temperature becomes slighter and slighter with time.

Porosity, Effective Pore Radius, and Permeability

The porous medium is the composite of solid framework and void. Inside granule-packed or sintered porous media there are netlike channels which diffuse fluid and heat in all directions. These processes occurring in porous media are different from those occurring in channels or pipelines so that some parameters are introduced to characterize the structure and properties of porous media. Among them, the permeability characterizes mass transfer in porous media, and the effective thermal conductivity characterizes heat transfer in porous media. Different from the effective thermal conductivity which is related to not only properties of the working fluid and solid framework but also the structure of porous media, porosity, effective pore/particle radius, and permeability are a set of interactive parameters which are only related to the porous structure. To the best of our knowledge, it has rarely been performed in the literature to consider the effect of coupled porosity, effective pore/particle radius, and permeability on the wick's performances at the same time [11,16,17], though the permeability is generally treated as the function of porosity and effective pore/particle radius. In this section, we focus on the effect of the permeability on the wick's performances. The change of the permeability can be realized by changing porosity or effective pore/particle radius, respectively, while the effective thermal conductivity remains unchanged by replacing the material that constructs the solid framework.

The relation among porosity, effective particle diameter, and permeability in sphere-particle porous media obeys the Blake–Kozeny equation [22,23]

$$K = \frac{d^2\phi^3}{120(1-\phi)^2} \tag{12}$$

where d is the effective particle diameter. According to the relation introduced in Eq. (12) and the relation between the particle radius and the pore radius introduced in [22,23], the relation among porosity,

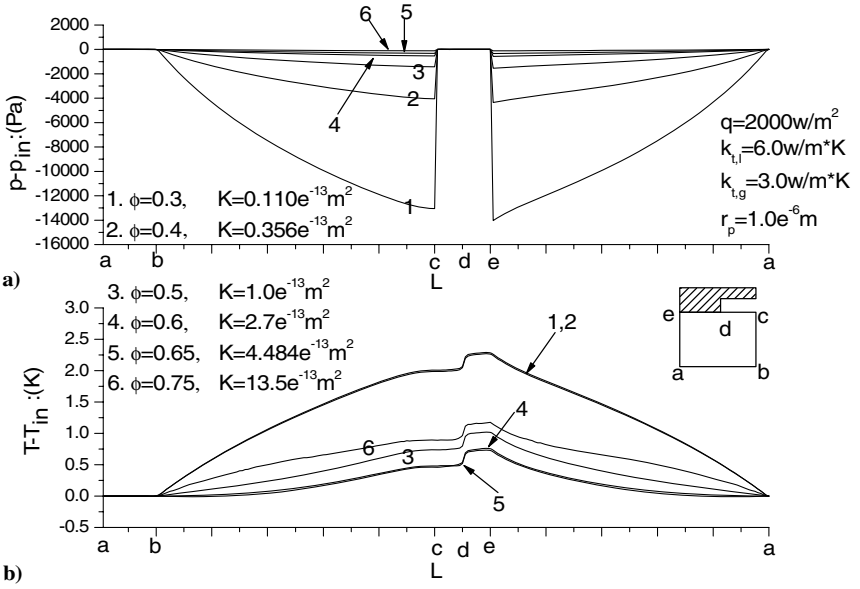

Fig. 6 Effect of porosity and permeability on a) pressure and b) temperature at $q = 2000$ W/m^2.

effective pore radius, and permeability applied to this paper is derived as

$$K = \frac{\phi^3 (6r_p)^2}{180(1-\phi)^2} \tag{13}$$

where r_p is the effective pore radius. In this paper, the fiducial permeability, $K = 10^{-13}$ m^2, with the effective pore radius of 0.001 mm and porosity of 0.5 is the experimental result of the nickel-sintered capillary wick. The value at the denominator in Eq. (13), which is equal to 180, is obtained by fitting the fiducial value of the porosity, effective pore radius, and permeability into Eq. (13).

Effect of Porosity and Permeability on Wick's Performances

The LHP is a self-driving device depending on heat flux. Heat flux leads to evaporation of the working fluid, and the capillary force at menisci formed by evaporation drives the working fluid flowing. Compared with other effects, heat flux determines primarily the magnitude of pressure and temperature. During heat transfer with flow and evaporation in the wick, there are three competing dynamic and thermodynamic processes: evaporation, heat conduction of the porous structure, and convection of the cool working liquid, among which evaporation occurs only on the interface. The combined effect of the three processes determines pressure, temperature, the position of the interface, the curvature of menisci, and so on.

Heat flux q obeys the following balance of energy:

$$qA_s = \dot{m}[c_{p,l}(T_{\text{eva}} - T_{\text{in}}) + \lambda + c_{p,g}(T_{\text{out}} - T_{\text{eva}})] + k_t \left.\frac{\partial T}{\partial r}\right|_{\text{in}} A_{\text{in}} \tag{14}$$

where A_s is the area of a close-contacted heated fin, A_{in} is the inlet area of the wick, T_{eva} is the evaporating temperature, and $\dot{m}$ is the mass flow rate. In Eq. (14), λ is the latent heat of evaporation and the other two terms in the square brackets are called sensible heat. The remaining right terms are the heat leak on the entrance. Combining Eqs. (2) and (14), considering the heat leak and sensible heat much smaller than latent heat, we predict that the smaller the permeability is, the greater the pressure drop and the capillary force (i.e., the curvature of menisci) are in the case of fixed heat flux. The effects of porosity and permeability on them are presented, respectively, in Figs. 6a and 7b at $q = 2000$ W/m^2, and in Figs. 8a and 9b at $q = 20,000$ W/m2. The numerical results agree well with the above prediction.

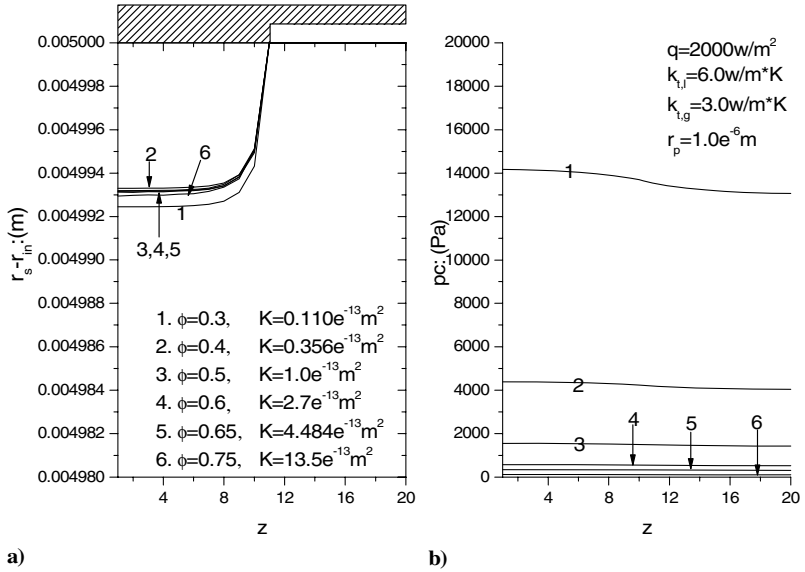

Fig. 7 Effect of porosity and permeability on a) the position of the interface and b) the capillary force at $q = 2000$ W/m^2.

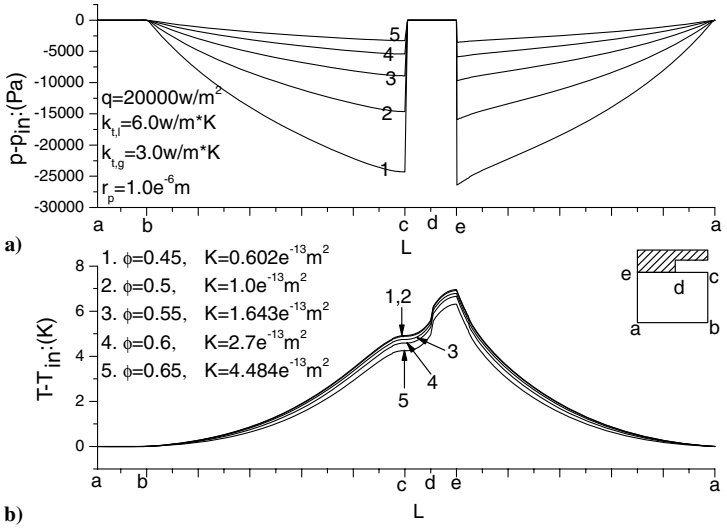

Fig. 8 Effect of porosity and permeability on a) pressure and b) temperature at $q = 20,000\ \mathrm{W/m^2}$.

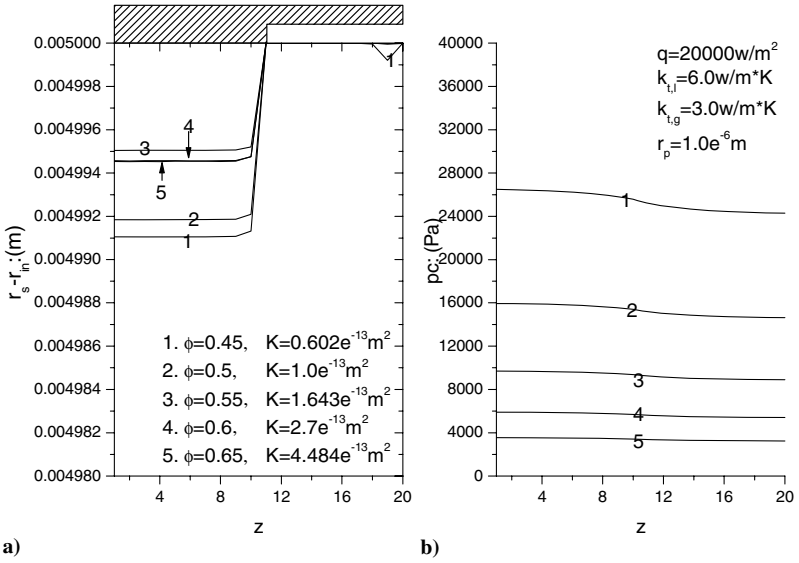

Fig. 9 Effect of porosity and permeability on a) the position of the interface and b) the capillary force at $q = 20,000\ \mathrm{W/m^2}$.

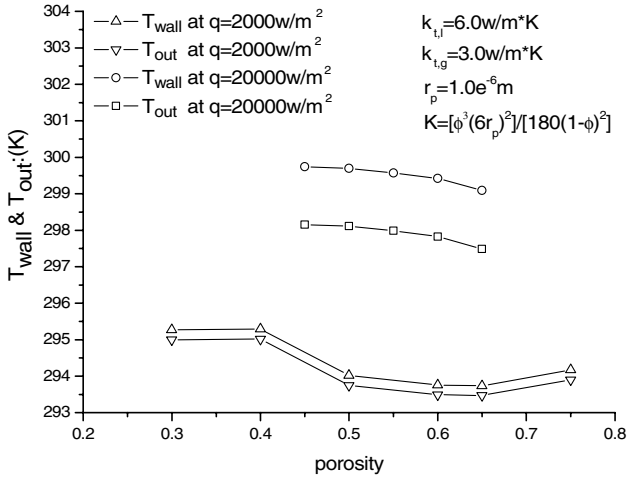

Fig. 10 Effect of porosity and permeability on mean fin temperature T_{wall} and mean outlet temperature T_{out}.

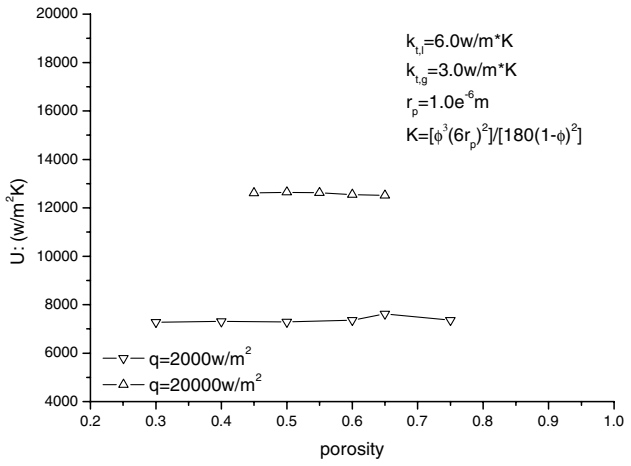

Fig. 11 Effect of porosity and permeability on the wick's total heat transfer coefficient.

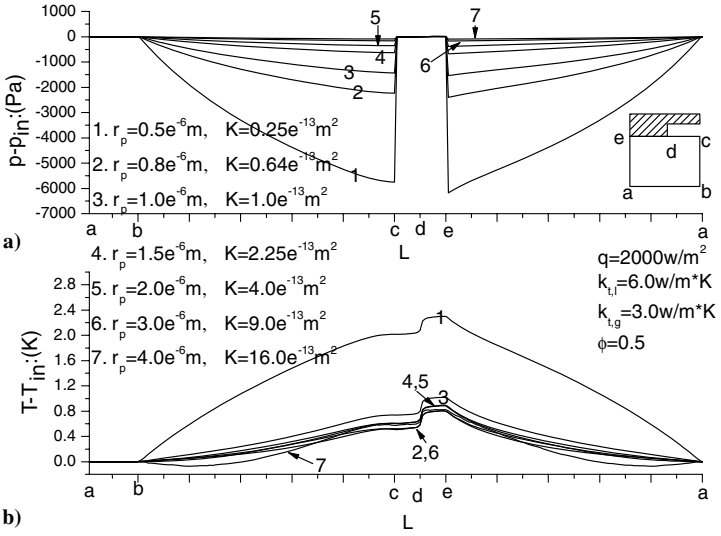

Fig. 12 Effect of effective pore radius and permeability on a) pressure and b) temperature at $q = 2000\ \mathrm{W/m^2}$.

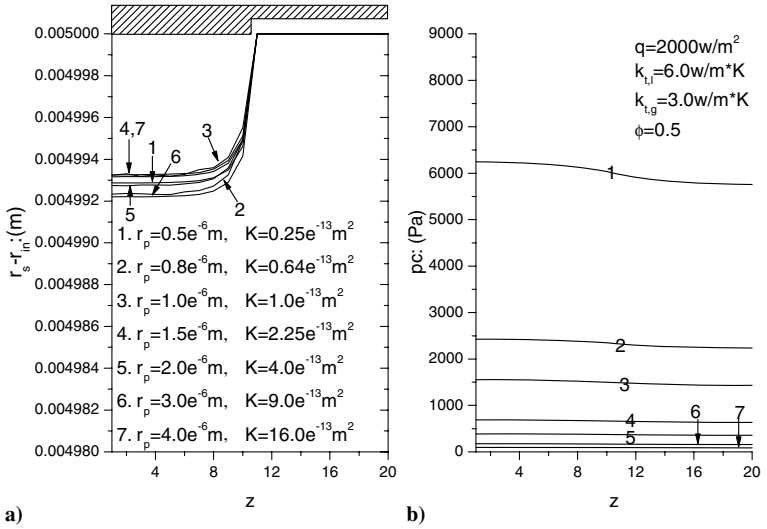

Fig. 13 Effect of effective pore radius and permeability on a) the position of the interface and b) the capillary force at $q = 2000\ \mathrm{W/m^2}$.

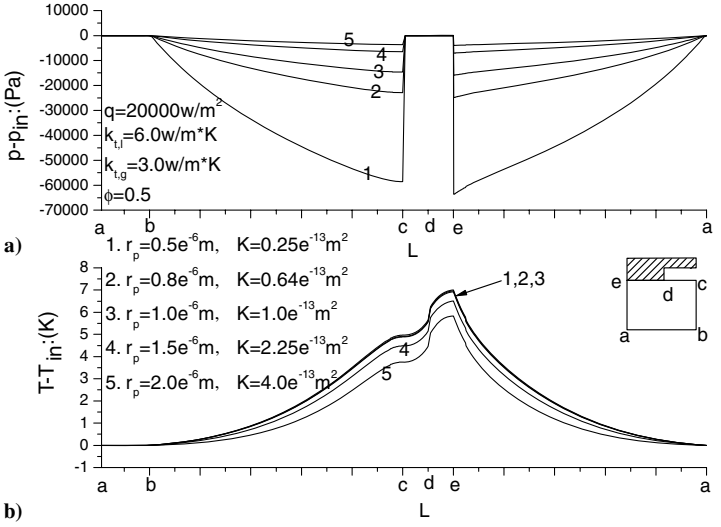

Fig. 14 Effect of effective pore radius and permeability on a) pressure and b) temperature at $q = 20,000\ \mathrm{W/m^2}$.

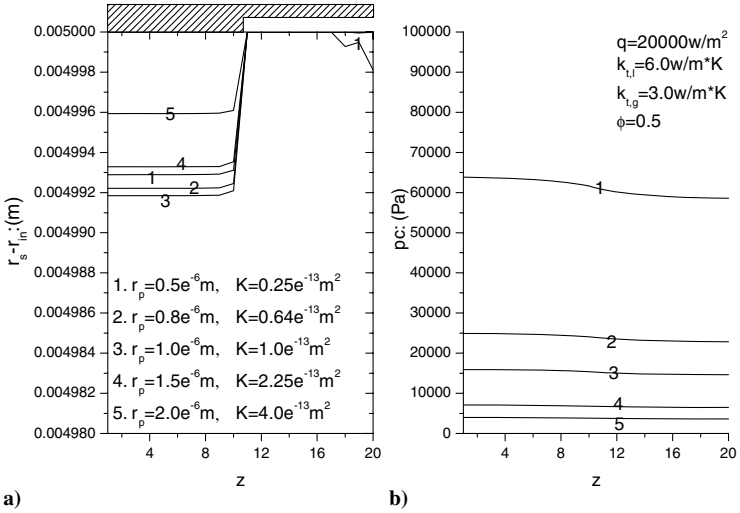

Fig. 15 Effect of effective pore radius and permeability on a) the position of the interface and b) the capillary force at $q = 20,000$ W/m^2.

Profiles of temperature with different porosity and permeability are presented in Fig. 6b at $q = 2000$ W/m2 and in Fig. 8b at $q = 20,000$ W/m2, respectively. Generally, the efficiency of convective heat transfer depends on the Reynolds number and the Prandtl number while the efficiency of conductive heat transfer is determined by the effective thermal conductivity. Because of the constant properties, the efficiency of convective heat transfer only depends on the velocity which is associated with heat flux and permeability, respectively, through Eqs. (2) and (14) so that it is determined primarily by heat flux and influenced secondly by permeability. The profiles of temperature along the boundaries a–e and b–c are convex in the case of dominant conductive heat transfer because the flowing area enlarges along the radius direction and concave in the case of dominant convective heat transfer due to the nonlinear effect of convection. As shown in Fig. 8b where convective heat transfer is dominant, the difference among profiles of temperature with different porosity and permeability is tiny though greater permeability is more favorable to flow and leads to lower temperature. As shown in the profiles (1)–(5) in Fig. 6b, temperature decreases monotonously with porosity and permeability increasing, and so does the heat leak on the entrance where the slope of the profile of temperature on the boundary a–b determines the heat leak there. The convex profile (1) in Fig. 6b is corresponding to the mode of dominant conductive heat transfer, whereas it is changed to the concave profile (5) which is corresponding to the mode in which convective heat transfer is comparative to conductive heat transfer, because the flow is weak due to the lower heat flux and sensitive to the change of permeability. On the contrary, temperature increases with porosity and permeability increasing after the permeability is greater than 4.484×10^{-13} m^2. This is because the too great permeability induces the tiny capillary force, and thus weakens convection.

The effects of porosity and permeability on the position of the interface are presented in Fig. 7a at $q = 2000$ W/m2 and Fig. 9a at $q = 20,000$ W/m2, respectively. As shown in Figs. 7a and 9a, movement of the interfaces is not monotonously changed. The heat flux "turns on" the LHP in aspects of not only evaporation but also the working fluid flowing. According to the previous discussion, there are three competing dynamic and thermodynamic processes: evaporation, heat conduction of the porous structure, and convection of the cool working liquid. Because the behavior of the interface includes both the position of the interface and the curvature of menisci on the interface, the effect of the interaction between the flowfield and the liquid–vapor interface lies in both aspects. Heat conduction of the porous structure transfers heat from the heated fin to the interface while convection of the cool working liquid transports liquid from the entrance to the interface. Evaporation makes use of both heat and liquid on the interface. The behavior of the interface is a result of the combined effect of evaporation, heat conduction, and convection. The vapor blanket invades more deeply into the wick when the effect of evaporation and heat conduction is stronger than the effect of convection, and it is pushed back when the effect of evaporation and heat conduction is weaker than the effect of convection.

Mean fin temperature T_{wall} and mean outlet temperature T_{out} with different porosity and permeability are presented in Fig. 10. Both mean temperatures decrease with porosity and permeability increasing when convective heat transfer is dominant, and they increase when convection is weak, which has already been explained. However, the difference between the mean temperatures changes little with the change of porosity and permeability.

Finally, the effect of porosity and permeability on the heat transfer efficiency is studied. The total heat transfer coefficient U of the capillary wick is defined as [13]

$$U = \frac{q}{T_{\text{wall}} - T_{\text{out}}} \tag{15}$$

The effect of porosity and permeability on the wick's total heat transfer coefficient is presented in Fig. 11. The coefficient depends on the effects of evaporation, heat conduction of the porous structure, and convection of the working fluid. Because of the previous assumption of keeping the effective thermal conductivity constant or numerically independent of porosity, effective pore radius, and permeability, porosity and permeability are not related to the former two processes. Although porosity and permeability do influence convection, they have little influence on the temperature difference between the fin and the outlet. Therefore they have little influence on the total heat transfer coefficient.

Effect of Effective Pore Radius and Permeability on Wick's Performances

The capillary force and pore radius obey the Young–Laplace equation, which is presented as

$$p_c = \frac{2\sigma}{R} = \frac{2\sigma \cos\theta}{r_p} \tag{16}$$

where σ is the coefficient of surface tension, R is the radius of menisci's curvature, and θ is the contact angle between the liquid and the solid surface. The maximum capillary force is obtained when $\theta = 0$. The effective pore radius has positive and negative influences on the wick's performances: On the one hand, due to smaller effective pore radius, greater maximum capillary force is obtained to prevent the vapor from invading more deeply into the wick, which enhances the capacity of the wick's accepting heat flux and "a hydraulic lock" [6]. On the other hand, smaller effective pore radius leads to smaller permeability that increases the flowing resistance,

which weakens the capacity of the wick's convective heat transfer and may result in too high temperature at which the LHP cannot work in the heat transfer mode and may be even damaged.

The effects of effective pore radius and permeability on pressure, temperature, the position of the interface, and the capillary force are presented in Figs. 12 and 13 at $q = 2000\ \mathrm{W/m^2}$, and in Figs. 14 and 15 at $q = 20,000\ \mathrm{W/m^2}$, respectively. The effect of them on mean temperatures T_{wall} and T_{out} is presented in Fig. 16. Greater effective pore radius and permeability lead to smaller pressure drop and capillary force, as well as a little lower temperature in the case of dominant convective heat transfer. As a result of the competing effect of evaporation, conductive, and convective heat transfer, the movement of interfaces does not change monotonously. The effective pore radius and permeability have little influence on the temperature difference between T_{wall} and T_{out}, as a result of which the total heat transfer coefficient hardly changes with the variation of the effective pore radius and permeability. These discussions are the same as those of the effect of porosity and permeability, which indicates that the effect of permeability on the wick's working state and performances is much more obvious than the effect of the maximum capillary force though both permeability and the maximum capillary force are the function of the effective pore radius.

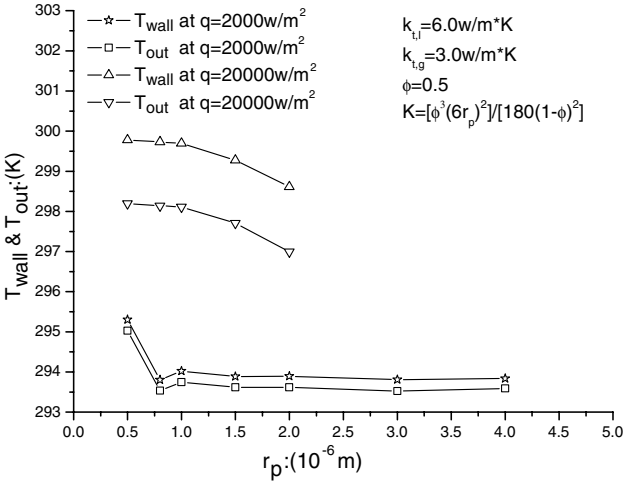

Fig. 16 Effect of effective pore radius and permeability on mean temperatures T_{wall} and T_{out}.

Heat Transfer Performance and Porous Structure Parameters

We redescribe the total heat transfer coefficient as the function of permeability in Fig. 17. As shown in Fig. 17, the total heat transfer coefficient has little change with permeability increasing. Furthermore, the line with different porosities and the line with different effective pore radii are superposed at the same heat flux, which indicates that the effect of permeability on the wick's working state and performances is the dominant factor while other effects of porosity or the effective pore radius is weak. From the results as shown in Fig. 17 as well as the similarity between these results in Figs. 6–10 and those in Figs. 12–16, we can see that it is sufficient for researchers/engineers to focus on the effect of permeability, which is considered as a function of porosity and the effective pore radius, in place of the effects of a set of porous structure parameters though the capillary force is related to the effective pore radius.

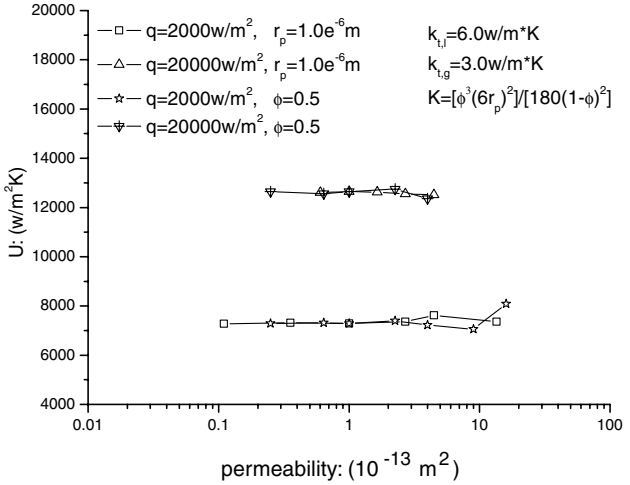

Fig. 17 Effect of permeability on the wick's total heat transfer coefficient.

Conclusions

An axisymmetric two-dimensional mathematical model, which considers adequately the capillary-driven convection as well as the effect of the interaction between the flowfield and the liquid–vapor interface on the position of the interface and the curvature of menisci, is developed to investigate the effect of porous structure parameters on wick's performances without gravity. In this paper, the relation among porosity, effective pore radius, and permeability is considered while the effective thermal conductivity is adjusted to be numerically independent of them.

The effect of permeability on the working state and performance is the dominant factor while other effects of porosity or the effective pore radius is weak. Because of permeability as a function of porosity and the effective pore/particle radius, it is sufficient for researchers/engineers to focus on the effect of permeability in place of the effects of a set of porous structure parameters. Permeability and the effective thermal conductivity should be the most interesting porous structure parameters.

Permeability has little influence on the heat transfer performance but has strong influence on the driving performance. Greater permeability enhances the capacity of convection and leads to smaller pressure drop and capillary force. At higher heat flux, the wick works in the mode of dominant convective heat transfer, and greater permeability leads to a little lower temperature; at lower heat flux, the wick works in the mode of dominant conductive heat transfer, and it is changed to the mode in which convective heat transfer is comparative to conductive heat transfer with the increment of permeability because the flow is weak and sensitive to the change of permeability.

Movement of the interfaces is not monotonously changed with permeability increasing. The behavior of the interface is a result of the combined effect of evaporation, heat conduction, and convection. The vapor blanket invades more deeply into the wick when the effect of evaporation and heat conduction is stronger than the effect of convection, and it is pushed back when the effect of evaporation and heat conduction is weaker than the effect of convection.

Appendix: Boundary Conditions

The boundary conditions with L_r and L_z standing for the radial thickness and the longitudinal width of a cell, respectively, are listed in the following. The saturated liquid lies on the entrance with $T_{\mathrm{in}} = 293$ K and $P_{\mathrm{in}} = 882,500$ Pa while the outlet pressure is simplified to the value of $P_{\mathrm{out}} = 882,500$ Pa.

1) When $z = 0$ or $z = L_z$ (the boundaries b–c and a–e in Fig. 2)

$$\frac{\partial T}{\partial z} = 0, \qquad \frac{\partial p}{\partial z} = 0 \tag{A1}$$

2) When $r = r_{\mathrm{in}}$ (the boundary a–b in Fig. 2)

$$T = T_{\mathrm{in}}, \qquad p = p_{\mathrm{in}} \tag{A2}$$

3) When $r = r_{\mathrm{out}} = r_{\mathrm{in}} + L_r$ and $0 < z < L_z/2$ (the boundary d–e in Fig. 2)

$$\begin{cases} \frac{\partial p}{\partial r} = 0, & \text{if the interface does not lie on the boundary d–e} \\ -\rho_f \frac{K}{\mu_f} \frac{\partial p}{\partial r}\Big|_l \lambda = q - k_t \frac{\partial T}{\partial r}\Big|_l, & \text{if the interface lies on the boundary d–e} \end{cases} \tag{A3}$$

$$\begin{cases} -k_t \frac{\partial T}{\partial r} = q, & \text{if the interface does not lie on the boundary d–e} \\ -k_t \frac{\partial T}{\partial r}\Big|_g = q, & \text{if the interface lies on the boundary d–e} \end{cases} \tag{A4}$$

4) When $r = r_{\text{out}} = r_{\text{in}} + L_r$ and $L_z/2 < z < L_z$ (the boundary c–d in Fig. 2)

$$\begin{cases} p = p_{\text{out}}, & \text{if the interface does not lie on the boundary c–d} \\ \rho_f \frac{K}{\mu_f} \frac{\partial p}{\partial r}\Big|_l \lambda = k_t \frac{\partial T}{\partial r}\Big|_l, & \text{if the interface lies on the boundary c–d} \end{cases} \tag{A5}$$

$$\begin{cases} \frac{\partial T}{\partial r} = 0, & \text{if the interface does not lie on the boundary c–d} \\ \frac{\partial T}{\partial r}\Big|_g = 0, & \text{if the interface lies on the boundary c–d} \end{cases} \tag{A6}$$

where λ is the latent heat of evaporation.

Acknowledgments

The authors would like to acknowledge the support of the Chinese Academy of Space Technology, National Natural Science Funding of China with Project No. 70601026, and the Chinese Academy of Science with a Dean Excellent Funding.

References

[1] Kaya, T., and Hoang, T. T., "Mathematical Modeling of Loop Heat Pipes and Experimental Validation," *Journal of Thermophysics and Heat Transfer*, Vol. 13, No. 3, 1999, pp. 14–320.

[2] Ku, J., "Operating Characteristics of Loop Heat Pipes," SAE Paper 1999-01-2007, 1999.

[3] Pouzet, E., Joly, J. L., Platel, V., Grandpeix, J. Y., and Butto, C., "Dynamic Response of a Capillary Pumped Loop Subjected to Various Heat Load Transients," *International Journal of Heat and Mass Transfer*, Vol. 47, Nos. 10–11, 2004, pp. 2239–2316.

[4] Zhang, H. X., Lin, G. P., Ding, T., Yao, W., Shao, X. G., Sudalov, R. G., and Maidanik Yu. F., "Investigation of Startup Behaviors of a Loop Heat Pipe," *Journal of Thermophysics and Heat Transfer*, Vol. 19, No. 4, 2005, pp. 509–518.

[5] Vasiliev, L. L., "Heat Pipes in Modern Heat Exchanges," *Applied Thermal Engineering*, Vol. 25, No. 1, 2005, pp. 1–19.

[6] Maydanik Y. F., "Loop Heat Pipes," *Applied Thermal Engineering*, Vol. 25, Nos. 5–6, 2005, pp. 635–657.

[7] Cao, Y., and Faghri, A., "Conjugate Analysis of a Flat-Plate Type Evaporator for Capillary Pumped Loops with Three-Dimensional Vapor Flow in the Groove," *International Journal of Heat and Mass Transfer*, Vol. 37, No. 3, 1994, pp. 401–409.

[8] Cao, Y., and Faghri, A., "Analytical Solutions of Flow and Heat Transfer in a Porous Structure with Partial Heating and Evaporation on the Upper Surface," *International Journal of Heat and Mass Transfer*, Vol. 37, No. 10, 1994, pp. 1525–1533.

[9] LaClair, T. J., and Mudawar, I., "Thermal Transients in a Capillary Evaporator Prior to the Initiation of Boiling," *International Journal of Heat and Mass Transfer*, Vol. 43, No. 21, 2000, pp. 3937–3952.

[10] Demidov, A. S., and Yatsenko, E. S., "Investigation of Heat and Mass Transfer in the Evaporation Zone of a Heat Pipe Operating by the 'Inverted Meniscus' Principle," *International Journal of Heat and Mass Transfer*, Vol. 37, No. 14, 1994, pp. 2155–2163.

[11] Khrustalev, D., and Faghri, A., "Heat Transfer in the Inverted Meniscus Type Evaporator at High Heat Fluxes," *International Journal of Heat and Mass Transfer*, Vol. 38, No. 16, 1995, pp. 3091–3101.

[12] Figus, C., Bray Y. L., Bories, S., and Prat, M., "Heat and Mass Transfer with Phase Change in a Porous Structure Partially Heated: Continuum Model and Pore Network Simulation," *International Journal of Heat and Mass Transfer*, Vol. 42, No. 14, 1999, pp. 2557–2569.

[13] Zhao, T. S., and Liao, Q., "On Capillary-Driven Flow and Phase-Change Heat Transfer in a Porous Structure Heated by a Finned Surface: Measurements and Modeling," *International Journal of Heat and Mass Transfer*, Vol. 43, No. 7, 2000, pp. 1141–1155.

[14] Kaya, T., and Goldak, J., "Numerical Analysis of Heat and Mass Transfer in the Capillary Structure of a Loop Heat Pipe," *International Journal of Heat and Mass Transfer*, Vol. 49, Nos. 17–18, 2006, pp. 3211–3220.

[15] Ren, C., Wu, Q. S., and Hu, M. B., "Heat Transfer with Flow and Evaporation in Loop Heat Pipe's Wick at Low or Moderate Heat Fluxes," *International Journal of Heat and Mass Transfer*, Vol. 50, Nos. 11–12, 2007, pp. 2296–2308.

[16] Liao, Q., and Zhao, T. S., "Evaporative Heat Transfer in a Capillary Structure Heated by a Grooved Block," *Journal of Thermophysics and Heat Transfer*, Vol. 13, No. 1, 1999, pp. 126–133.

[17] Hanlon, M. A., and Ma, H. B., "Evaporative Heat Transfer in Sintered Porous Media," *Journal of Heat Transfer—Transaction of ASME*, Vol. 125, No. 4, 2003, pp. 644–652.

[18] Ren, C., and Wu, Q. S., "Heat Transfer in Loop Heat Pipe's Wick: Effect of Effective Thermal Conductivity," *Journal of Thermophysics and Heat Transfer*, Vol. 21, No. 1, 2007, pp. 134–140.

[19] Udell, K. S., "Heat Transfer in Porous Media Heated from Above with Evaporation, Condensation and Capillary Effects," *Journal of Heat Transfer—Transaction of ASME*, Vol. 105, No. 3, 1983, pp. 485–492.

[20] Zeng D. L., Ao, Y., Zhu, K. X., and Li, Q. R., *Engineering Thermophysics*, High Education Press, Beijing, China, 1985, pp. 191–199 (in Chinese).

[21] Tao, W. Q., *Neoteric Advance in Numerical Heat Transfer*, Science Press, Beijing, China, 2001, pp. 233–237, 283–286 (in Chinese).

[22] Lin, T. R., *Introduction to Heat and Mass Transfer in Porous Media*, Science Press, Beijing, China, 1995, p. 303 (in Chinese).

[23] Cotter, T. P., "Theory of Heat Pipe," USAEC Report No. LA-3246, Los Alamos Scientific Lab, University of California, 1965.